

Tuning Band Gap and Work Function Modulations in Monolayer hBN/Cu(111) Heterostructures with Moiré Patterns

Qiang Zhang,^{†,‡,§,▽,||} Jin Yu,^{||,⊥,▽,||} Philipp Ebert,^{#,||} Chendong Zhang,^{§,□} Chi-Ruei Pan,[○] Mei-Yin Chou,^{○,¶} Chih-Kang Shih,^{*,§,||} Changgan Zeng,^{*,†,‡,||} and Shengjun Yuan^{*,□,||}

[†]International Center for Quantum Design of Functional Materials (ICQD), Hefei National Laboratory for Physical Sciences at the Microscale, and Synergetic Innovation Center of Quantum Information and Quantum Physics, University of Science and Technology of China, Hefei, Anhui 230026, China

[‡]CAS Key Laboratory of Strongly-Coupled Quantum Matter Physics, and Department of Physics, University of Science and Technology of China, Hefei, Anhui 230026, China

[§]Department of Physics, University of Texas at Austin, Austin, Texas 78712, United States

^{||}Beijing Computational Science Research Center, Beijing 100084, China

[⊥]Theory of Condensed Matter, Radboud University, Nijmegen 6525, AJ, The Netherlands

[#]Peter Grünberg Institut, Forschungszentrum Jülich GmbH, 52425 Jülich, Germany

[□]School of Physics and Technology, Wuhan University, Wuhan 430072, China

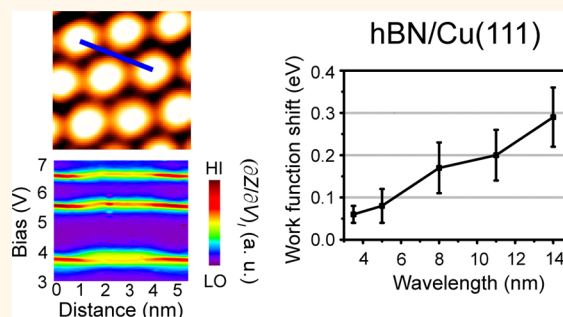
[○]School of Physics, Georgia Institute of Technology, Atlanta, Georgia 30332, United States

[¶]Institute of Atomic and Molecular Sciences, Academia Sinica, Taipei 10617, Taiwan

Supporting Information

ABSTRACT: The moiré pattern formed between a two-dimensional (2D) material and the substrate has played a crucial role in tuning the electronic structure of the 2D material. Here, by using scanning tunneling microscopy and spectroscopy, we found a moiré-pattern-dependent band gap and work function modulation in hexagonal boron nitride (hBN)/Cu(111) heterostructures, whose amplitudes increase with the moiré pattern wavelength. Moreover, the work function modulation shifts agree well with the conduction band edge shifts, indicating a spatially constant electron affinity for the hBN layer. Density functional theory calculations showed that these observations in hBN/Cu(111) heterostructures mainly originated from the hybridization of the N 3p_z orbital and Cu 4s orbital in different atomic configurations. Our results show that the twist-angle dependence of moiré patterns in hBN/Cu(111) heterostructures can be used to tailor the electronic properties including band gap and work function.

KEYWORDS: hexagonal boron nitride, moiré pattern, scanning tunneling microscopy and spectroscopy, band gap, work function, density functional theory



Two-dimensional materials have attracted increasing attention since the first successful exfoliation of single-layer graphene,¹ owing particularly to the prospect of taking advantage of their exceptional electronic properties in novel devices. This requires the ability to design 2D materials with optimized properties. An effective way of tuning the physical properties of 2D materials is building heterostructures. Due to lattice mismatch and relative orientation, heterostructures of 2D materials mostly exhibit moiré patterns. These moiré patterns provide periodic potentials and thereby affect

the electronic structures of these 2D materials. Such examples have been shown recently for several cases: One example is graphene on hexagonal boron nitride (hBN), where the moiré potential gives rise to the superlattice Dirac points^{2–5} and the self-similar Hofstadter butterfly states.^{6,7} Another example is a very recent finding that suggests that strongly correlated states

Received: June 12, 2018

Accepted: August 14, 2018

Published: August 14, 2018

(Mott insulators and superconductors) can be realized in twisted bilayer graphene by precisely tuning the rotation angle between the layers.^{8,9} Besides graphene, it was found recently that the moiré pattern formed in the transition metal dichalcogenide heterobilayer can be used to create a lateral 2D electronic superlattice as well.^{10–12}

A single atomic insulating hBN layer grown on transition metal (TM) substrates^{13–15} (e.g., Ru, Ir, Cu) also exhibits moiré patterns, reflecting the local variations of atomic alignment between hBN and the TM substrate. It has been shown that such moiré patterns lead to periodic modulations of the work function,^{16–19} which can be harnessed as a “nanoscale electrostatic trapper of single molecules”.²⁰ In addition, the hBN/TMs system has become an important platform for the templated growth of molecular layers or heterostructures.^{19,21,22}

It is noted that the interaction between the hBN layer and the TM substrate can vary greatly. For example, the interaction is quite strong in hBN/Ru(0001) or hBN/Rh(111), resulting in a significant amount of charge transfer between the hBN layer and the TM substrate.¹⁹ On the other hand, the interaction is rather weak in hBN/Cu(111),^{23–25} yet the system exhibits a large work function modulation amplitude.^{17,26} This presents an *apparent paradox*: Since the work function modulation is presumably due to the local variations of the charge transfer, why does the weakly coupled hBN/Cu(111) system exhibit an even larger work function modulation than the strongly coupled hBN/Ru(0001) system? Another critical, but totally unexplored question is whether the band gap of hBN can also exhibit periodic modulations following the moiré patterns, similar to that observed in a van der Waals vertical heterostructure discovered recently.¹⁹

In this work, by utilizing the twist-angle dependence of the moiré pattern, we explore the tunability of the electronic properties (specifically work function and band gap modulations) of single-monolayer hBN on Cu(111). In this weakly interacting system, the moiré pattern wavelength λ is governed by the twist angle ϕ between the hBN single layer and the Cu(111) surface: It changes from 14 nm for $\phi \approx 0^\circ$ to 3.5 nm for $\phi \approx 4^\circ$. We use scanning tunneling microscopy and spectroscopy (STM/S) to probe the spatial variations of the work function and the band gap as a function of the moiré pattern wavelength. We find a spatial modulation of the work function with an amplitude ranging from 0.3 eV for $\lambda = 14$ nm to a negligible value for $\lambda = 3.5$ nm. In addition, the band gap of hBN also exhibits a spatial modulation, whose amplitude depends on the moiré wavelength, too, decreasing from 0.48 eV for $\lambda = 14$ nm to 0.27 eV for $\lambda = 3.5$ nm. Our results provide a recipe to design the desired band gap and work function of an hBN monolayer, by suitably adjusting the moiré pattern using the twist angle between a monolayer and the weakly interacting substrate. This methodology may help to optimize the electronic properties of a wide variety of 2D materials exhibiting moiré patterns for future device applications.

RESULTS AND DISCUSSION

Electronically Corrugated Topography in hBN/Cu(111) Heterostructures. The morphology of an hBN monolayer on Cu(111) is dominated by moiré patterns with varying wavelengths ranging from 3.5 to 14 nm. The STM image in Figure 1a illustrates one example of such a moiré pattern morphology of hBN/Cu(111). On the right side is a

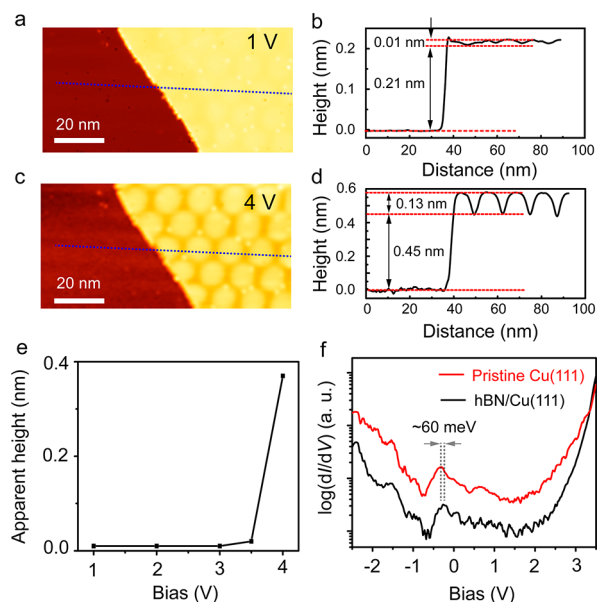


Figure 1. Sample bias dependence of constant-current STM images. (a, c) Large-scale STM images (100 nm \times 50 nm) of the partially covered hBN/Cu(111) sample taken at sample voltages of +1 V and +4 V, respectively. The right terrace is covered by a monolayer hBN, while the left one is a lower pristine Cu(111) terrace. (b, d) Line profiles along the dotted lines in (a) and (c), respectively. The step height increases from 0.22 nm at +1 V (a) to 0.58 nm at +4 V (c). Simultaneously, the amplitude of the moiré pattern increases from almost negligible to 0.13 nm. These observations demonstrate that the image contrast is dominated by electronic modulation instead of structure modulation of the hBN overlayer. (e) The apparent height of hBN as a function of the sample bias indicates that the CBM of the hBN layer is at around +3.5 V. (f) dI/dV spectra taken on the pristine Cu(111) and hBN/Cu(111) surfaces with a sample stabilization voltage of +3.5 V. The energy of the interface state is shifted upward by only about 60 meV in the presence of the hBN overlayer, indicating the weak interaction between hBN and the Cu(111) surface.

Cu(111) terrace covered by a monolayer hBN sheet, while on the left side is a lower pristine Cu(111) terrace. A comparison of the STM images acquired at +1 V and +4 V in Figure 1a and c shows that the image contrast is highly dependent on the sample bias. The height profiles in Figure 1b and d demonstrate that the step height increases from 0.22 nm (corresponding to the Cu(111) layer separation) at +1 V to 0.58 nm at +4 V. Simultaneously, the amplitude of the moiré patterns increases from an almost negligible height modulation (0.01 nm) at +1 V to 0.13 nm at +4 V. These observations demonstrate that the image contrast of the hBN overlayer is dominated by the electronic modulation instead of the structure modulation. The bias-dependent STM images acquired at some other biases are also shown in Figure S1, and the apparent height of the hBN layer as a function of the sample bias is plotted in Figure 1e. Note that when the bias is within the band gap of hBN, the image contrast between the pristine Cu region and the Cu region with an hBN layer on top is negligible (about 0.01 nm), since electrons in the tip tunnel into the Cu electronic states. On the other hand, once the bias is moved into the conduction band (CB) region of hBN, the tip immediately moves back to reflect mostly the topographic contrast. Therefore, the bias-dependent STM images shown in Figures 1 and S1 provide an important clue that the energy

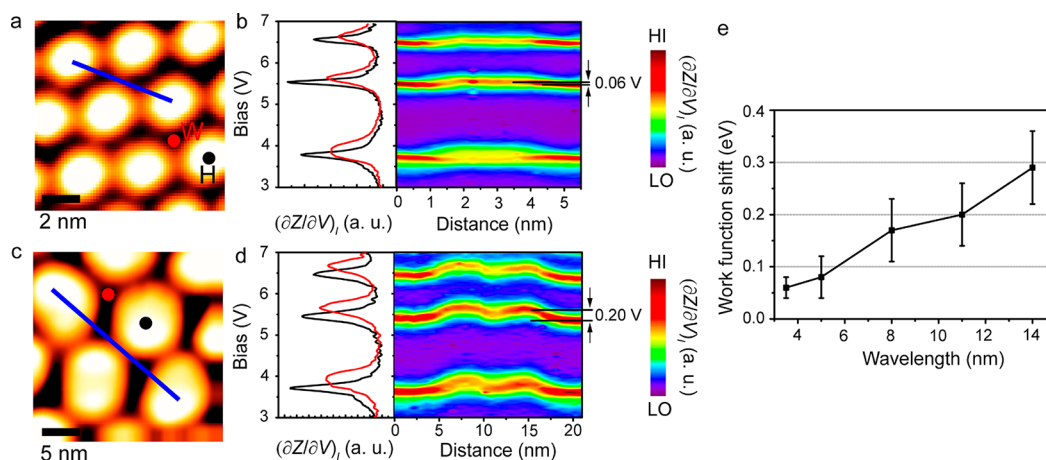


Figure 2. Spatial modulation of FERs for hBN with different moiré patterns. (a, c) STM images of the moiré pattern with 3.5 and 11 nm periodicity, respectively. The scanning biases of these two STM images are +4 V. (b, d) The left panels show typical FER spectra taken from the wire (red) and hole (black) regions. The contour plots in the right panel show spatial mapping of the $(\partial Z/\partial V)_I$ spectra. The peak positions (appear in red) shift to a higher sample bias from the hole to the wire, indicating an energy shift of the work function. The amplitude of this spatial modulation of the peak energy locations increases from 0.06 ± 0.02 eV for a 3.5 nm moiré pattern to 0.2 ± 0.06 eV for the moiré pattern with an 11 nm periodicity. (e) The work function shift as a function of the moiré wavelength clearly shows that the work function modulation amplitude increases with the moiré pattern wavelength. The error bars in energy represent the standard deviation.

location of the conduction band minimum (CBM) of hBN is at around +3.5 V.

In addition, Figure 1f shows the tunneling spectra acquired on the pristine Cu(111) and hBN/Cu(111) surfaces with a sample stabilization voltage of +3.5 V (around the energy location of the CB edge). We observed in tunneling spectra the presence of an interface state with an energy close to the surface state of the pristine Cu(111) surface. The energy of this interface state is shifted upward by only about 60 meV in the presence of hBN. This indicates that the Cu surface below the hBN layer essentially remains intact and the influence of hBN on the Cu(111) surface is rather weak, in agreement with a previous report.¹⁷ This weak interaction is further confirmed by our observations of different moiré patterns appearing in hBN films on Cu(111).

Work Function Modulation in hBN/Cu(111) Heterostructures. Figure 2a and c show STM images of hBN/Cu(111) with two different moiré patterns with wavelengths of 3.5 and 11 nm, respectively. Following previous studies of hBN on TMs, two distinct regions in hBN/Cu(111) were defined: The strongly bound region and the loosely bound region are labeled as “hole” (H) and “wire” (W) in the STM image in Figure 2a, respectively. The left panels in Figure 2b and d display the corresponding $(\partial Z/\partial V)_I$ spectra measured at the hole and wire regions. The peaks in the $(\partial Z/\partial V)_I$ spectra reflect the field emission resonances (FERs).²⁷ Such FERs have been utilized to determine the local work function in several systems including hBN grown on several different TMs.^{17–19} One can see that the peaks in the $(\partial Z/\partial V)_I$ spectra are shifted to a much higher sample bias in the wire region compared to that in the hole region. We acquired a series of $(\partial Z/\partial V)_I$ spectra along the blue lines indicated in Figure 2a and c and mapped the $(\partial Z/\partial V)_I$ signal as a function of the spatial position in a contour plot (high intensity appears in red), as shown in the right panels of Figure 2b and d. Following the previous studies, we use the second-order FERs to precisely determine the relative shifts of the work function, as it is supposed to be less influenced by the image potential.^{18,28} Nevertheless, we notice that in our case all three FER

resonances shown here have nearly identical modulation amplitudes. A clear modulation of the peak energy locations can be recognized for the 11 nm moiré pattern with an amplitude of 0.20 eV. In sharp contrast, the energy modulation is much weaker (0.06 eV) for the hBN sheet with a moiré wavelength of 3.5 nm.

On this basis, we also measured the work function shifts for the other three moiré patterns (see Figure S2) and then plotted the work function shift as a function of the moiré wavelength in Figure 2e. It is found that the measured amplitude of the spatial modulation of the work function increases with the moiré wavelength.

Band Gap Modulation in hBN/Cu(111) Heterostructures. In addition to the work function modulation, we observed a band gap modulation as well, e.g., in dI/dV spectra acquired along the same spatial line as indicated in Figure 2c. In Figure 3a, one can clearly observe a large band gap for hBN/Cu(111) when the tunneling spectra were acquired with a relatively large sample stabilization voltage of +5 V (implying a relatively large sample-to-tip distance). The spectra in Figure 3a reveal that the band gap of hBN in the wire region is larger compared to that found in the hole region (note that the dI/dV spectra are displayed in a logarithmic scale to better identify the band edges). Furthermore, the spatial mapping of the differential conductivity for a moiré pattern with an 11 nm periodicity in Figure 3b demonstrates that the conduction and valence band edges and the corresponding band gap exhibit a pronounced spatial modulation.

However, a quantitative determination of the band gap, CBM, and valence band maximum (VBM) energy locations of hBN based on STS measurements needs to be handled with care. We note that a detailed angle-resolved photoemission spectroscopy (ARPES) investigation on hBN/Cu(111) has been carried out previously.²⁹ The VBM location of hBN was determined at 2.95 ± 0.05 eV below the Fermi energy. Nevertheless, in that work, ARPES was not able to reveal the periodic modulation of the VBM location due to the moiré pattern as discussed in our work. In our measurement (Figure 3a), the VBM of hBN in the hole region is determined at about

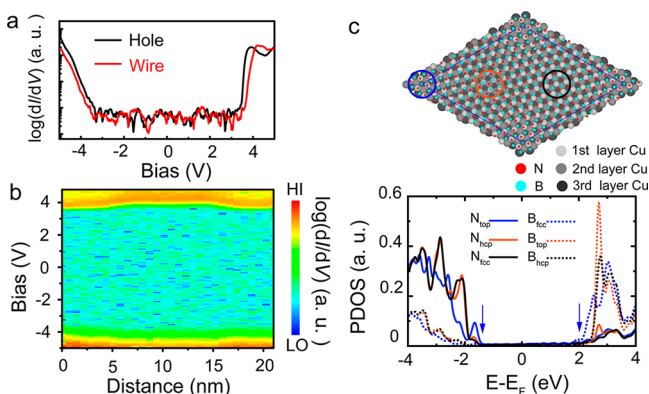


Figure 3. Spatial mapping of the tunneling spectra and the calculated projected densities of states (PDOS). (a) Typical $\log(dI/dV)$ spectra taken from the wire (red) and hole (black) regions as indicated in Figure 2c, respectively. The band gap is larger in the wire region compared to that in the hole region (stabilization voltage: $V_b = +5$ V, current: $I = 60$ pA). (b) Contour plot of $\log(dI/dV)$ along the blue line in Figure 2c, clearly illustrating the spatial modulation of the band gap and band edges. (c) (Upper panel) Top view of a supercell containing $\sqrt{139} \times \sqrt{139}$ hBN/ $\sqrt{133} \times \sqrt{133}$ Cu(111) that we used to simulate a 2.96 nm moiré pattern. The red and light blue spheres represent nitrogen and boron atoms, respectively. The first, second, and third layer of Cu atoms are illustrated by gray spheres with different size and darkness. High-symmetry regions of $B_{fcc}N_{top}$, $B_{top}N_{hcp}$, and $B_{hcp}N_{fcc}$ are marked by blue, orange, and black circles, respectively. (Lower panel) The PDOS for the p orbitals of B atoms (dashed lines) and N atoms (solid lines) in different regions are shown with the energy zero set at the Fermi level. The CB edge derives primarily from the B p orbitals and the VB edge from the N p orbitals. One can see that the CB edge in the region containing N atoms (shown by the blue dashed line) on the top site (labeled as $B_{fcc}N_{top}$) shifts down by about 0.4 eV, while the first peak shifts down by about 0.2 eV. The blue vertical arrows indicate the band edges of the hBN layer.

3.15 ± 0.1 eV below the Fermi energy. So the two different measurements (STS *versus* ARPES) are consistent within the experimental errors. Although this might suggest a systematic error in our determination of the VBM location of ~ 0.2 eV, it does not affect our conclusion regarding the *relative* change of the VBM location between the hole and wire regions. For the determination of the CBM location, one does not have ARPES as a reference anymore. In this case, as discussed previously (see Figure 1, Figure S1, and the related discussions), the CBM determined by the bias-dependent STM images is at around +3.5 V. On the other hand, the CBM of hBN in the hole region determined by STS is at about 3.46 ± 0.1 eV above the Fermi energy. These two values are consistent, further confirming the validity of our CBM locations. Therefore, the discussions above verify one of the most important conclusions in the current work: the VBM/CBM energy locations and the band gap modulation within the moiré pattern.

In order to capture the behavior of the band gap modulation in a specific moiré pattern, we performed first-principles calculations on the electronic properties of one possible configuration of the hBN/Cu(111) supercell. Shown in the upper panel of Figure 3c is the top view of the supercell containing $\sqrt{139} \times \sqrt{139}$ hBN/ $\sqrt{133} \times \sqrt{133}$ Cu(111), which is used to model a 2.96 nm moiré pattern with a twist angle of 4.75° . The average height of the hBN layer above the Cu surface from our supercell calculation is 3.21 Å, which agrees

well with the values of 3.24 \AA^{24} and 3.38 \AA^{25} obtained from the X-ray standing wave (XSW) experiments. In the lower panel, the projected densities of states (PDOS) for the p orbitals of B and N atoms in different regions are shown with the energy zero set at the Fermi level. The CB edge derives primarily from the B p orbitals and the VB edge from the N p orbitals. One can see that the CB edge in the region containing N atoms on the top site (labeled as $B_{fcc}N_{top}$, shown by the blue dashed line) shifts down by about 0.4 eV (marked by a vertical blue arrow), while the first peak shifts down by about 0.2 eV. The $B_{fcc}N_{top}$ site corresponds to the center of the hole site in the STM image shown in Figure 2a, while the other two correspond to the wire sites. Simultaneously, at the $B_{fcc}N_{top}$ site the projected N states show an extra small peak near the VB edge, leading to a higher VB edge than those in the other two configurations. This small peak near the VBM in the hole region ($B_{fcc}N_{top}$) may be detected in tunneling measurements through its stronger coupling with the Cu orbitals in this geometry. Thus, the band edges marked by the two blue arrows indicate a band gap narrowing in the hole region compared to the other two regions, which agree well with our experimental results.

In Figure 4 we show the energy differences of the VB edge, the CB edge, and the work function between the hole and wire

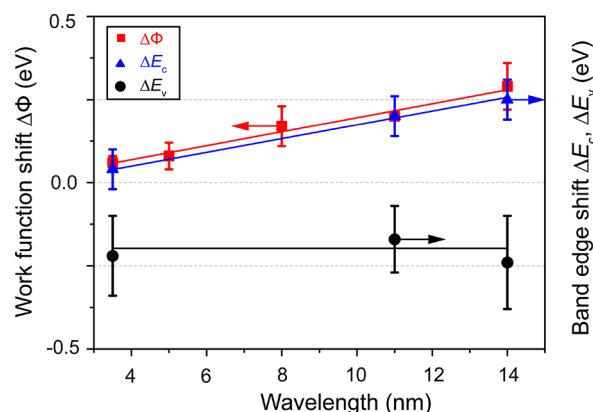


Figure 4. Work function and band edge shifts as a function of the moiré pattern wavelength. The solid lines represent linear fits of the data points shown in the same color. The conduction band edge shifts in phase with identical amplitude as the work function shift (compare red and blue symbols). They both increase linearly with the moiré pattern wavelength, whereas the valence band edge shift is constant. The error bars in energy represent the standard deviation.

regions as a function of the moiré pattern wavelength. Two interesting features are detectable:

(i) The energy differences of the CB edge exhibit the same trend and magnitude variation with the wavelength as that of the work function. The linear fitting of the energy shifts of the work function (red line) and the CB edge (blue line) are identical within the error bars. This similarity indicates a spatially unchanged electron affinity χ for hBN: The work function is given by $\Phi = E_{vac} - E_F = \chi + E_C - E_F$, with E_{vac} , E_F , and E_C being the vacuum level, Fermi level, and CBM. Hence, if Φ and $E_C - E_F$ exhibit the same spatial modulation, χ remains spatially constant.

(ii) On the other hand, we experimentally observed that the VB edge exhibits a constant shift around 0.2–0.3 eV, which is independent of the moiré pattern wavelength. One probable origin of this independence is due to the dominating N–Cu

interaction. In the wire region where the N atoms are away from the top sites, the hybridization is the weakest, and no new state is formed near the VB edge. But in the hole region, the N atom sits directly above a Cu atom (N_{top}) and exhibits the strongest orbital interaction with the metal orbitals, forming additional features slightly above the VB edge, which induces a spatial modulation of the VB edge. The calculated energy of the small new peak for N_{top} is about 0.4 eV higher than the peaks in other regions, consistent with the measured VB edge modulation of 0.2–0.3 eV. Our speculation is that this strong feature is quite local; therefore it is less sensitive to the moiré pattern wavelength.

We next discuss the moiré pattern wavelength dependence of the work function and band gap modulation within the moiré pattern. Our theoretical results based on the supercell with $\lambda = 2.96$ nm show negligible work function modulation (<0.1 eV). Experimentally, at $\lambda = 3.5$ nm, we detect also only a very weak modulation amplitude of 0.06 eV. Interestingly, for the strongly interacting system of hBN/Ru(0001) with $\lambda \approx 3$ nm, the same supercell method yields a substantial work function modulation of ~ 0.15 eV, consistent with the experimental observation in that system.¹⁹ Performing first-principles calculations using plane waves on the supercell with a moiré pattern wavelength far beyond 3 nm, however, is technically formidable. In order to capture the origin of these experimental observations, a modified approach is adopted by building periodical unit cells capturing the local structure of the moiré pattern, in which we can perform accurate calculations on the local electronic properties. As the 1×1 unit cell is created based on the local structure of the moiré pattern, it can capture the local electronic properties for different stacking configurations.^{30,31} Here, we set the lattice constant of pristine hBN and Cu(111) to be 2.504 and 2.553 Å, respectively, and the moiré pattern originates from both lattice mismatch and relative orientation. Consequently, we obtain the moiré pattern wavelength and orientation as a function of the twist angle ϕ between stretched hBN and Cu(111) as shown in Figure 5a. When the twist angle between hBN and Cu(111) decreases from 30° to 0° , the calculated wavelength of the moiré pattern increases from 0.49 nm to 14.9 nm, among which the largest moiré pattern corresponds to a 57×57 hBN on a 56×56 Cu(111) supercell. Figure 5b shows the simulated atomic structure of hBN on Cu(111) with a rotation angle of about 0.8° . The moiré pattern is clearly visible with a wavelength of 11 nm, which is in good agreement with the experimentally observed case in Figure 2c.

As indicated, in the hole center the N atom is located on top of the surface Cu atom, forming a $B_{\text{fcc}}N_{\text{top}}$ structure. Here, the strongest bonding originates from the hybridization of the $3p_z$ orbital of N and $4s$ orbital of Cu. It will form a relative strong bond with energy $V_{\text{sp}\sigma}$ and leads to the strongest charge transfer, as shown in Figure 5c. This will introduce a much lower ground state energy in N, as it has new components from the free electron in Cu due to hybridization, leading to a narrower band gap. On the contrary, B and N atoms have various configurations in the wire region. As an example, they are located above the hollow sites of two closest Cu triangles, forming a $B_{\text{hcp}}N_{\text{fcc}}$ structure. In this case, the hybridization is the weakest and the bond energy becomes $V_{\text{sp}\sigma} \cos \theta$, where θ is the angle between the vertical line and the vector connecting N and Cu atoms. This weakest bonding leads to the fact that all the electronic properties of this kind of BN structures should be less affected by Cu and will be closer to the pristine BN.

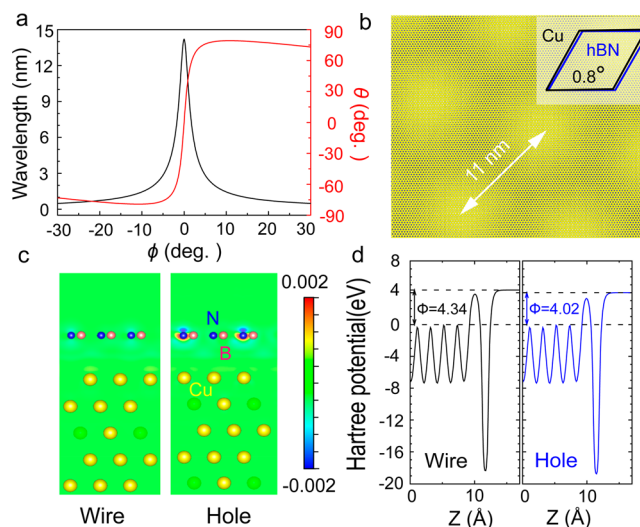


Figure 5. DFT calculations for the hBN moiré pattern. (a) Wavelength (black) and rotation (red) of the moiré pattern as a function of the rotation angle between the stretched hBN and Cu(111) lattices. (b) Calculated hBN atomic structure of the 11 nm moiré pattern. (c) Slice of charge transfer between the hBN and Cu(111). The charge transfer is stronger in the hole regions compared to the wire regions. The charge transfer unit is $e/\text{Å}^3$. (d) Calculated Hartree potential variations in the hole and wire positions, respectively.

The modified density functional theory (DFT) calculation is based on a 1×1 unit cell for the two different configurations: one adopting the $B_{\text{fcc}}N_{\text{top}}$ structure and the other one the $B_{\text{hcp}}N_{\text{fcc}}$ structure. In Figure 5d, we plot the plane-averaged Hartree potential along the vertical direction. This modified 1×1 unit-cell approach is probably valid for moiré patterns with a long wavelength, since the local $B_{\text{fcc}}N_{\text{top}}$ or $B_{\text{hcp}}N_{\text{fcc}}$ structures are more extended. Indeed, the calculation shows a local work function difference of about 0.3 eV between the hole and wire regions (4.02 eV versus 4.34 eV), which is in agreement with those reported previously using 1×1 unit cells.^{17,25} This 1×1 approach also yields a band gap difference of ~ 0.5 eV between $B_{\text{fcc}}N_{\text{top}}$ and $B_{\text{hcp}}N_{\text{fcc}}$ structures.

Experimentally, we find that as the moiré pattern wavelength is reduced, the work function modulation amplitude is also reduced. Theoretically, the supercell approach leads to a negligible work function modulation for $\lambda = 2.96$ nm, whereas the modified 1×1 unit-cell approach leads to an appreciable work function modulation of ~ 0.3 eV. Each of these two approaches contains its own limitations: The supercell approach is limited to the short-wavelength regime ($\lambda \leq 3$ nm), while the modified 1×1 unit-cell approach is applicable for only the long-wavelength limit. Together they are consistent with the experimental observation that the work function modulation is negligible at short wavelength and becomes appreciable at long wavelength.

This result may appear puzzling at first sight, since the amount of charge transfer (maximum at the $B_{\text{fcc}}N_{\text{top}}$ site, the so-called hole region, and minimum at the $B_{\text{hcp}}N_{\text{fcc}}$ and $B_{\text{top}}N_{\text{hcp}}$ sites, the so-called wire region) would be independent of the moiré wavelength. However, on closer examination, we found this is actually the result expected, as the electrostatic potential at a particular location depends not only on the local charge but also on the charge distribution nearby. Considering that the local work function measurement is obtained using

FER in the STM setup, with a typical tip-to-sample separation exceeding 1 nm, the electrostatic potential $V(r)$ includes the contributions from the charge distribution in the neighboring area of several nanometers. When the wavelength is short, the charge distribution varies quickly in the effective region. As a result, the local electrostatic potential would be smaller than that of a uniformly distributed charge density. Conversely, when the wavelength is long, then the local electrostatic potential would be closer to that for a uniformly distributed charge density. In the [Supporting Information](#), we provide a more detailed discussion including model calculations using a uniformly charged disc and Gaussian charge distribution of finite diameter as an illustration (see [Figure S3](#) and the detailed description in the [Supporting Information](#)). This realization of wavelength-dependent work function modulation amplitude also resolves the apparent paradox discussed earlier. For the strongly interacting hBN/Ru(0001) system, the moiré pattern occurs primarily at $\phi \approx 0^\circ$ with $\lambda = 3.2$ nm and the work function modulation is about 0.15 eV. In comparison, for the weakly coupled hBN/Cu(111) system with moiré pattern of a similar wavelength ($\lambda = 3.5$ nm for $\phi \approx 4^\circ$), the work function modulation amplitude is negligible, although for a moiré pattern wavelength of 11 nm, the work function modulation amplitude increases significantly to 0.2 eV.

CONCLUSIONS

In summary, we systematically investigated the moiré pattern wavelength-dependent work function and band gap modulations in hBN/Cu(111) heterostructures. When the Cu(111) surface is covered by hBN, due to the interlayer interaction, the work function of the system is reduced compared to the bare Cu(111) surface. The work function modulation is mainly contributed by the hybridization of N $3p_z$ and Cu $4s$ orbitals with a bonding energy of $V_{sp\sigma} \cos \theta$. When the N atom sits right on top of a Cu atom in the hole region, the hybridization is the strongest; when the N atom sits between two Cu atoms in the wire region, the hybridization is the weakest. The wavelength dependence of the modulation amplitude can be understood by considering that the local work function is derived from electrostatic contributions of a region on the order of nanometers beyond a single atomic site. In addition, we discovered that the band gap of the insulating hBN atomic layer also exhibits similar modulation. This can be understood by considering that the CBM and VBM of the system are mainly contributed by the p_z orbitals of boron and nitrogen atoms, respectively. Furthermore, the band gap of hBN can be modulated by the wavelength of the moiré pattern as well. In general, we mimic the mechanism of the work function shift in the hBN/Cu(111) heterostructure and emphasize the role of the moiré pattern wavelength played in tuning the electronic properties. We would expect our results to be helpful in studying the electronic properties of moiré patterns in other 2D materials.

METHODS

Growth of hBN/Cu(111) Heterostructures. The clean Cu(111) surface was obtained by repeated cycles of Xe^+ sputtering (1 kV) followed by annealing at 800 °C. A partial coverage of an hBN monolayer was formed on Cu(111) when the single crystal was heated to 800 °C and exposed to a borazine vapor of 5×10^{-5} Torr for about 5 min; then the sample was slowly cooled to room temperature.

Scanning Tunneling Microscopy and Spectroscopy. All STM investigations reported here were acquired at 77 K in ultrahigh vacuum (base pressure is better than 6×10^{-11} Torr). Electrochemically etched tungsten tips were cleaned *in situ* with electron beam bombardment. The bias voltage was applied to the sample. Current–voltage (I – V) and dI/dV spectra were acquired at a constant tip-to-sample distance Z with the feedback loop off. The $(\partial Z/\partial V)$ spectrum was acquired when the tip-to-sample distance Z changes corresponding to the scanning of bias V in order to keep the constant current.

Theoretical Calculations. Our theoretical calculations were performed using the Vienna *ab Initio* simulation package (VASP)^{32,33} with the projector augmented wave method.^{34,35} The supercell consists of $\sqrt{139} \times \sqrt{139}$ hBN on $\sqrt{133} \times \sqrt{133}$ Cu(111) with a twist angle of 4.75° , giving rise to a 2.96 nm moiré pattern. The slab contains three layers of Cu atoms and a vacuum region of about 15 Å. A plane-wave cutoff energy of 400 eV was used, and only the gamma point was sampled. The optB86b functional including the van der Waals correction³⁶ was adopted for the structural relaxation. The structure was fully relaxed until the force on each atom was smaller than 0.01 eV \AA^{-1} .

Considering that the STM measurement gives the local electronic states of the heterostructure, we use a unit cell based on the atomic structure of a certain area in one specific moiré pattern to study the electronic properties locally. The structure is chosen as a repeated structure at the hole and wire center of the moiré pattern. A five-atom-thick Cu(111) layer is modeled as the substrate with the top two-atom layers as buffering layers. The Brillouin zone sampling was done using a $15 \times 15 \times 1$ Monkhorst–Pack grid for both structure relaxation and static calculations.³⁷ All the atoms in the unit cell were fully relaxed until the force on each atom was less than 0.01 eV/\AA . Electronic minimization was performed with a tolerance of 10^{-5} eV. Differential charge was defined as $\rho = \rho_{\text{hBN/Cu}} - \rho_{\text{hBN}} - \rho_{\text{Cu}}$, where $\rho_{\text{hBN/Cu}}$, ρ_{hBN} , and ρ_{Cu} represent the charge density of the hBN/Cu system, single hBN sheet, and Cu substrate, respectively.

ASSOCIATED CONTENT

Supporting Information

The Supporting Information is available free of charge on the ACS Publications website at DOI: [10.1021/acsnano.8b04444](https://doi.org/10.1021/acsnano.8b04444).

Additional experimental STM and model calculation data ([PDF](#))

AUTHOR INFORMATION

Corresponding Authors

*E-mail: shih@physics.utexas.edu.

*E-mail: cgzeng@ustc.edu.cn.

*E-mail: s.yuan@whu.edu.cn.

ORCID

Qiang Zhang: 0000-0002-1788-9243

Jin Yu: 0000-0003-1074-2465

Philipp Ebert: 0000-0002-2022-2378

Chih-Kang Shih: 0000-0003-2734-7023

Changgan Zeng: 0000-0001-8630-845X

Author Contributions

Q. Zhang and J. Yu contributed equally to this work.

Notes

The authors declare no competing financial interest.

ACKNOWLEDGMENTS

This research was supported by the National Key R&D Program of China (Grant No. 2017YFA0403600), the National Basic Research Program of China (Grant No. 2014CB921102), National Natural Science Foundation of China (Grant No. 11434009 and No. 11461161009), and

Anhui Initiative in Quantum Information Technologies. J.Y. and S.J.Y. acknowledge the computational resources and financial support from Beijing Computational Science Research Center (NSAF U1530401) and the financial support from the European Research Council Advanced Grant Program (Contract No. 338957). C.D.Z. acknowledges support from the National Natural Science Foundation of China (Grant No. 11774268). C.-R.P. and M.-Y.C. acknowledge support from Academia Sinica (AS-106-TP-A07) and the U.S. National Science Foundation (NSF) (EFMA-1542747). C.-K.S. thanks the Welch Foundation (F-1672) and the U.S. National Science Foundation (NSF) (EFMA-1542747). S.J.Y. acknowledges support from the Thousand Young Talent Plan and the National Natural Science Foundation of China (Grand No. 11774269).

REFERENCES

- (1) Novoselov, K. S.; Geim, A. K.; Morozov, S. V.; Jiang, D.; Katsnelson, M. I.; Grigorieva, I. V.; Dubonos, S. V.; Firsov, A. A. Two-Dimensional Gas of Massless Dirac Fermions in Graphene. *Nature* **2005**, *438*, 197–200.
- (2) Park, C.-H.; Yang, L.; Son, Y.-W.; Cohen, M. L.; Louie, S. G. New Generation of Massless Dirac Fermions in Graphene Under External Periodic Potentials. *Phys. Rev. Lett.* **2008**, *101*, 126804.
- (3) Yankowitz, M.; Xue, J.; Cormode, D.; Sanchez-Yamagishi, J. D.; Watanabe, K.; Taniguchi, T.; Jarillo-Herrero, P.; Jacquod, P.; LeRoy, B. J. Emergence of Superlattice Dirac Points in Graphene on Hexagonal Boron Nitride. *Nat. Phys.* **2012**, *8*, 382–386.
- (4) Ponomarenko, L. A.; Gorbachev, R. V.; Yu, G. L.; Elias, D. C.; Jalil, R.; Patel, A. A.; Mishchenko, A.; Mayorov, A. S.; Woods, C. R.; Wallbank, J. R.; Mucha-Kruczynski, M.; Piot, B. A.; Potemski, M.; Grigorieva, I. V.; Novoselov, K. S.; Guinea, F.; Fal'ko, V. I.; Geim, A. K. Cloning of Dirac Fermions in Graphene Superlattices. *Nature* **2013**, *497*, 594–597.
- (5) Wang, E.; Lu, X.; Ding, S.; Yao, W.; Yan, M.; Wan, G.; Deng, K.; Wang, S.; Chen, G.; Ma, L.; Jung, J.; Fedorov, A. V.; Zhang, Y.; Zhang, G.; Zhou, S. Gaps Induced by Inversion Symmetry Breaking and Second-Generation Dirac Cones in Graphene/Hexagonal Boron Nitride. *Nat. Phys.* **2016**, *12*, 1111–1115.
- (6) Hunt, B.; Sanchez-Yamagishi, J. D.; Young, A. F.; Yankowitz, M.; LeRoy, B. J.; Watanabe, K.; Taniguchi, T.; Moon, P.; Koshino, M.; Jarillo-Herrero, P.; Ashoori, R. C. Massive Dirac Fermions and Hofstadter Butterfly in a van der Waals Heterostructure. *Science* **2013**, *340*, 1427–1430.
- (7) Yu, G. L.; Gorbachev, R. V.; Tu, J. S.; Kretinin, A. V.; Cao, Y.; Jalil, R.; Withers, F.; Ponomarenko, L. A.; Piot, B. A.; Potemski, M.; Elias, D. C.; Chen, X.; Watanabe, K.; Taniguchi, T.; Grigorieva, I. V.; Novoselov, K. S.; Fal'ko, V. I.; Geim, A. K.; Mishchenko, A. Hierarchy of Hofstadter States and Replica Quantum Hall Ferromagnetism in Graphene Superlattices. *Nat. Phys.* **2014**, *10*, 525–529.
- (8) Cao, Y.; Fatemi, V.; Demir, A.; Fang, S.; Tomarken, S. L.; Luo, J. Y.; Sanchez-Yamagishi, J. D.; Watanabe, K.; Taniguchi, T.; Kaxiras, E.; Ashoori, R. C.; Jarillo-Herrero, P. Correlated Insulator Behaviour at Half-Filling in Magic-Angle Graphene Superlattices. *Nature* **2018**, *556*, 80–84.
- (9) Cao, Y.; Fatemi, V.; Fang, S.; Watanabe, K.; Taniguchi, T.; Kaxiras, E.; Jarillo-Herrero, P. Unconventional Superconductivity in Magic-Angle Graphene Superlattices. *Nature* **2018**, *556*, 43–50.
- (10) Tong, Q.; Yu, H.; Zhu, Q.; Wang, Y.; Xu, X.; Yao, W. Topological Mosaics in Moiré Superlattices of van der Waals Heterobilayers. *Nat. Phys.* **2017**, *13*, 356–362.
- (11) Yu, H.; Liu, G.-B.; Tang, J.; Xu, X.; Yao, W. Moiré Excitons: From Programmable Quantum Emitter Arrays to Spin-Orbit-Coupled Artificial Lattices. *Sci. Adv.* **2017**, *3*, 1701696.
- (12) Zhang, C.; Chuu, C.-P.; Ren, X.; Li, M.-Y.; Li, L.-J.; Jin, C.; Chou, M.-Y.; Shih, C.-K. Interlayer Couplings, Moiré Patterns, and 2D Electronic Superlattices in MoS₂/WSe₂ Hetero-bilayers. *Sci. Adv.* **2017**, *3*, 1601459.
- (13) Corso, M.; Auwärter, W.; Muntwiler, M.; Tamai, A.; Greber, T.; Osterwalder, J. Boron Nitride Nanomesh. *Science* **2004**, *303*, 217–220.
- (14) Goriachko, A.; He, Y.; Knapp, M.; Over, H.; Corso, M.; Brugger, T.; Berner, S.; Osterwalder, J.; Greber, T. Self-Assembly of a Hexagonal Boron Nitride Nanomesh on Ru(0001). *Langmuir* **2007**, *23*, 2928–2931.
- (15) Laskowski, R.; Blaha, P.; Gallauner, T.; Schwarz, K. Single-Layer Model of the Hexagonal Boron Nitride Nanomesh on the Rh(111) Surface. *Phys. Rev. Lett.* **2007**, *98*, 106802.
- (16) Gómez Díaz, J.; Ding, Y.; Koitz, R.; Seitsonen, A. P.; Iannuzzi, M.; Hutter, J. Hexagonal Boron Nitride on Transition Metal Surfaces. *Theor. Chem. Acc.* **2013**, *132*, 1350.
- (17) Joshi, S.; Ecija, D.; Koitz, R.; Iannuzzi, M.; Seitsonen, A. P.; Hutter, J.; Sachdev, H.; Vijayaraghavan, S.; Bischoff, F.; Seufert, K.; Barth, J. V.; Auwärter, W. Boron Nitride on Cu(111): An Electronically Corrugated Monolayer. *Nano Lett.* **2012**, *12*, 5821–5828.
- (18) Schulz, F.; Drost, R.; Hämäläinen, S. K.; Demonchaux, T.; Seitsonen, A. P.; Liljeroth, P. Epitaxial Hexagonal Boron Nitride on Ir(111): A Work Function Template. *Phys. Rev. B: Condens. Matter Mater. Phys.* **2014**, *89*, 235429.
- (19) Zhang, Q.; Chen, Y.; Zhang, C.; Pan, C.-R.; Chou, M.-Y.; Zeng, C.; Shih, C.-K. Bandgap Renormalization and Work Function Tuning in MoSe₂/hBN/Ru(0001) Heterostructures. *Nat. Commun.* **2016**, *7*, 13843.
- (20) Dil, H.; Lobo-Checa, J.; Laskowski, R.; Blaha, P.; Berner, S.; Osterwalder, J.; Greber, T. Surface Trapping of Atoms and Molecules with Dipole Rings. *Science* **2008**, *319*, 1824–1826.
- (21) Schulz, F.; Drost, R.; Hämäläinen, S. K.; Liljeroth, P. Templated Self-Assembly and Local Doping of Molecules on Epitaxial Hexagonal Boron Nitride. *ACS Nano* **2013**, *7*, 11121–11128.
- (22) Joshi, S.; Bischoff, F.; Koitz, R.; Ecija, D.; Seufert, K.; Seitsonen, A. P.; Hutter, J.; Diller, K.; Urgel, J. I.; Sachdev, H.; Barth, J. V.; Auwärter, W. Control of Molecular Organization and Energy Level Alignment by an Electronically Nanopatterned Boron Nitride Template. *ACS Nano* **2014**, *8*, 430–442.
- (23) Preobrajenski, A. B.; Vinogradov, A. S.; Mårtensson, N. Monolayer of h-BN Chemisorbed on Cu(111) and Ni(111): The Role of the Transition Metal 3d States. *Surf. Sci.* **2005**, *582*, 21–30.
- (24) Brülke, C.; Heepenstrick, T.; Humberg, N.; Krieger, I.; Sokolowski, M.; Weiß, S.; Tautz, F. S.; Soubatch, S. Long Vertical Distance Bonding of the Hexagonal Boron Nitride Monolayer on the Cu(111) Surface. *J. Phys. Chem. C* **2017**, *121*, 23964–23973.
- (25) Schwarz, M.; Riss, A.; Garnica, M.; Ducke, J.; Deimel, P. S.; Duncan, D. A.; Thakur, P. K.; Lee, T.-L.; Seitsonen, A. P.; Barth, J. V.; Allegretti, F.; Auwärter, W. Corrugation in the Weakly Interacting Hexagonal-BN/Cu(111) System: Structure Determination by Combining Noncontact Atomic Force Microscopy and X-ray Standing Waves. *ACS Nano* **2017**, *11*, 9151–9161.
- (26) Koitz, R.; Seitsonen, A. P.; Iannuzzi, M.; Hutter, J. Structural and Electronic Properties of a Large-Scale Moiré Pattern of Hexagonal Boron Nitride on Cu(111) Studied with Density Functional Theory. *Nanoscale* **2013**, *5*, 5589–5595.
- (27) Gundlach, K. H. Zur Berechnung Des Tunnelstroms Durch Eine Trapezförmige Potentialstufe. *Solid-State Electron.* **1966**, *9*, 949–957.
- (28) Lin, C. L.; Lu, S. M.; Su, W. B.; Shih, H. T.; Wu, B. F.; Yao, Y. D.; Chang, C. S.; Tsong, T. T. Manifestation of Work Function Difference in High Order Gundlach Oscillation. *Phys. Rev. Lett.* **2007**, *99*, 216103.
- (29) Roth, S.; Matsui, F.; Greber, T.; Osterwalder, J. Chemical Vapor Deposition and Characterization of Aligned and Incommensurate Graphene/Hexagonal Boron Nitride Heterostack on Cu(111). *Nano Lett.* **2013**, *13*, 2668–2675.

(30) Laskowski, R.; Blaha, P.; Schwarz, K. Bonding of Hexagonal BN to Transition Metal Surfaces: An *ab initio* Density-Functional Theory Study. *Phys. Rev. B: Condens. Matter Mater. Phys.* **2008**, *78*, 045409.

(31) Bokdam, M.; Brocks, G.; Katsnelson, M. I.; Kelly, P. J. Schottky Barriers at Hexagonal Boron Nitride/Metal Interfaces: A First-Principles Study. *Phys. Rev. B: Condens. Matter Mater. Phys.* **2014**, *90*, 085415.

(32) Kresse, G.; Furthmüller, J. Efficiency of *ab initio* Total Energy Calculations for Metals and Semiconductors Using a Plane-Wave Basis Set. *Comput. Mater. Sci.* **1996**, *6*, 15–50.

(33) Kresse, G.; Furthmüller, J. Efficient Iterative Schemes for *ab initio* Total-Energy Calculations Using a Plane-Wave Basis Set. *Phys. Rev. B: Condens. Matter Mater. Phys.* **1996**, *54*, 11169–11186.

(34) Blöchl, P. E. Projector Augmented-Wave Method. *Phys. Rev. B: Condens. Matter Mater. Phys.* **1994**, *50*, 17953–17979.

(35) Kresse, G.; Joubert, D. From Ultrasoft Pseudopotentials to the Projector Augmented-Wave Method. *Phys. Rev. B: Condens. Matter Mater. Phys.* **1999**, *59*, 1758–1775.

(36) Klimeš, J.; Bowler, D. R.; Michaelides, A. Van der Waals Density Functionals Applied to Solids. *Phys. Rev. B: Condens. Matter Mater. Phys.* **2011**, *83*, 195131.

(37) Monkhorst, H. J.; Pack, J. D. Special Points for Brillouin-Zone Integrations. *Phys. Rev. B* **1976**, *13*, 5188–5192.